An Adaptive Approach to Non-Destructive Evaluation (NDE) of Cast Irons containing Precipitated Graphite Particles with the Help of Magnetoacoustic Emission

L. Piotrowski[1] and J. Sertucha[2]

1 Institute of Nanotechnology and Materials Engineering, Faculty of Applied Physics and Mathematics, Gdansk University of Technology, Narutowicza 11/12, 80-233 Gdansk, Poland

2 Azterlan, Basque Research and Technology Alliance, Aliendalde Auzunea 6, E-48200 Durango (Bizkaia), Spain

Corresponding author:

Leszek Piotrowski,

Institute of Nanotechnology and Materials Engineering, Faculty of Applied Physics and Mathematics, Gdansk University of Technology, Narutowicza 11/12, 80-233 Gdańsk, Poland

Tel: +(48 58) 348 66 17 , Fax: (+48 58) 347 28 21

E-mail address: lespiotr@pg.edu.pl

Abstract

Physical properties of cast irons strongly depend on both their microstructure and the presence of casting defects. The paper analyses the possibility of application of magnetoacoustic emission (MAE) for nondestructive detection of flawed cast iron components. The investigated samples containing dross, chunky graphite and lamellar graphite were compared with the reference, flawless, spheroidal cast iron sample. The optimisation adaptive procedure was applied for sensitivity enhancement. Application of five different acoustic emission sensors and filtering band optimisation enabled finding the optimum sensor/band configuration allowing not only for flawed samples identification, but also for discerning various kinds of flaws.

Keywords:

Cast iron, dross, chunky graphite, nondestructive testing, magnetoacoustic emission.

1. Introduction

Cast irons [1] include an interesting group of metallic alloys with important applications in different industry sectors such as automotive, wind mills, machinery, shipping, valves, etc. Although more limited than steels, the use of cast irons is also extensive all around the world showing important advantages due to their castability, low production costs, friendly as-cast shaping of castings, low risk

of shrinkage formation, fact that heat treatment is typically not needed to obtain the required microstructure and mechanical properties, etc. The main characteristics of cast iron alloys is the presence of graphite particles precipitated during solidification step which can adopt different shapes. Among them lamellas and nodules lead to lamellar or "grey" cast irons and to nodular or "ductile" cast irons, respectively [2].

As expected, physical properties of cast irons strongly depend on both their microstructure and the presence of casting defects. This last issue has been recently reviewed by Sertucha and Lacaze [3] and among the wide variety of defects inclusions and graphite degenerations are found to be two of the most common problems detected in as-produced castings. More precisely, those casting defects which do not show external signals, directly observable by the operators, make quite difficult their detection without additional and expensive investigations. In this sense, dross inclusions [3, 4] and chunky graphite [5] (CHG), both commonly found in heavy-section ductile iron castings, are two examples of this problematic issue regarding foundry plants.

Dross defects mainly correspond to Mg-O-Si compounds formed during turbulent fillings of big castings which need long solidification times. This defect is found as complex and irregular networks included into the metallic matrix and rarely achieves the skin of the casting. For the CHG, the origin of this defect is totally different being a graphite degeneration of spheroidal shape [6]. Although it shows different forms, the most common one corresponds to areas occupied by interconnected strings of graphite [7]. Both Dross and CHG negatively affect mechanical properties of castings and can make them unacceptable for customers, leading to relevant increases of scrap level and production costs.

The use of non-destructive techniques (NDT) like magnetic particles, or alternatively magnetic flux leakage (MFL) and ultrasound (US) testing enable detecting internal defects in cast iron castings and offers an interesting feedback when managing the quality control of products. Magnetic particles/MFL methods are both very useful for the surface or subsurface defect detection, yet they are not sensitive to bulk changes. The US show promise for the detection of microstructural changes [8] - it seems to be sensitive to spheroidicity level of graphite yet its usefulness for the detection of other flaws in graphite morphology is yet to be proven.

Another group of methods is based on analysis of magnetisation process of ferromagnetic materials: magnetic adaptive testing (MAT) [9], incremental permeability and magnetoacoustic emission (MAE) measurements. Two first methods are based on magnetic hysteresis loop measurements and both can be very sensitive to microstructural features of material, yet rather than competitive to the MAE they can be thought of as complementary methods.

The present work describes an NDT approach to a comparative investigation of four different cast iron alloys with the help of magnetoacoustic emission. The MAE phenomenon was for the first time well described by Lord [11] in 1975. It was then recognized as a potential NDT tool in 1981 by Shibata

2

and Ono [12]. It has already been shown that the MAE signal is strongly dependent on the microstructural features such as dislocation density [13, 14], carbide morphology [15], or phase composition of steel [16]. The MAE is a phenomenon of acoustic pulse generation during domain wall (DW) irreversible jumps in ferromagnetic materials. It is dependent on the local volume change, hence requires materials with non-zero magnetostriction [17]. Discontinuity of motion of DWs is a result of their interaction with pinning sites such as e.g. graphite particles. Graphite particles are much bigger than carbides in steels, hence one can expect complicate closure domain structures to be creates around them. There are two types of DWs - 180° and non 180° (90°in ferrous materials), where the angle is measured between magnetisation directions in adjacent domains. Only the movement of non 180° DWs results in the MAE pulse generation because the magnetostriction phenomenon is an even effect—i.e. two antiparallel domains are equally elongated. What is important, the method based on the MAE signal measurements analyses acoustic pulses (of ultrasound frequency) which are relatively weakly attenuated in steels, hence we can obtain information from the inside of the material.

The main difference in the results obtainable by hysteresis loop based methods and the MAE measurements is due to the fact that MAE is sensitive only to 90° DW. The methods based on hysteresis loops are sensitive to both kinds of cast iron DWs but the 180° ones are usually responsible for significantly greater change of magnetisation. Being so the highest absolute change of permeability is usually observed for magnetisation levels different from those for which the MAE signal is strongest. Being so, parallel application of those methods might increase the range of their application.

Thera are also some problems with hysteresis based methods even though not unsurmountable ones. The MAT method is very sensitive for the magnetising yoke and sample contact quality. If the contact quality changes e.g. due to small change of sample shape, resultant change of investigated parameter might be greater than the one caused by microstructure. The problem may by greatly reduced by applying air gap or separators between the electromagnet and sample and worsening the contact quality for all the samples. As for the incremental permeability method the local hysteresis loops are generated using high frequency component (kHz range) of magnetising current. It is necessary as in this case instead of points (in H-B space) we have to determine reversal hysteresis loops corresponding to those points. Such frequency makes the magnetisation of material difficult. The difficulty is due to eddy current generation and resultant bulk material screening. As a result it may prove problematic to investigate the bulk material structure in the case of greater dimensions of the investigated sample.

The MAE is not so strongly sensitive to the pole/sample contact quality since it is observed for lower differential permeability for which the dependence of magnetisation rate on the contact quality is significantly smaller. In addition to that, the MAE signals can be measured for low frequencies (smaller than 1Hz) for which there is usually no problem with magnetisation of bulk materials.

2. Experimental

One lamellar graphite cast iron alloy (LGI) and three different spheroidal cast iron alloys (SGI) were prepared for the investigations. For the second type, composition of the cast alloys was modified so as to obtain samples with Dross inclusions (SGI-Dross), with Chunky graphite (SGI-CHG) and another one free of any casting defect (SGI-nd).

Base melt batches were prepared in a medium frequency electric furnace (250 Hz, 100 kW) with 100-120 kg in capacity. In all cases the metallic charges were composed of about 50% steel bars and about 50% ductile iron returns. Once the melting processes were accomplished, the composition of each prepared batch was checked and then adjusted adding the corresponding products. Special care was taken to correct the carbon and silicon contents by using a high purity graphite (>98.9 wt.%) and a FeSi75 alloy (grain size 10-90 mm, Si = 75.2, Ca = 0.26, Al = 0.86, C = 0.13 and Fe balance, wt.%). The melt temperature was then increased up to 1450-1470ºC or 1500-1520ºC for the LGI or SGI alloys, respectively, and the slag obtained on the liquid alloy was finally removed.

The validated melts were transferred to a 50 kg capacity ladle then used for pouring the moulds in case of the LGI alloy. For the SGI alloys, this ladle was used to carry out the nodularization treatments by the tundish cover method (1450-1470ºC). For that purpose, 600 g (about 1.2 wt.% of the transferred melt weight) of a FeSiMg alloy (grain size 2–10 mm, Si = 45.9, Mg = 5.7, Ca = 2.42, Al = 0.39, rare earth elements (RE) = 2.24 and Fe balance, wt.%) were introduced in a chamber present in the bottom of the ladle, being then covered, first, with about 200 g of steel scrap (grain size 7–15 mm) and, then, with 100 g of a commercial inoculant (grain size 0.2-0.7 mm, Si = 69.9, Al = 0.93, Ca = 1.38, Bi = 0.49, RE = 0.37 and Fe balance, wt.%).

When the spheroidizing treatments for the SGI alloys were finished or once the LGI alloy was transferred from the furnace to the ladle, each of these batches was used to pour two chemically-bonded sand moulds at about 1370-1400ºC and thus produced two Y2 wedges with the LGI alloy and two Y3 wedges [18] per SGI alloy. In case of the Y3 wedges, the moulds were completely surrounded with an isolating cover just after pouring them. About 90 min after pouring, all cast wedges were removed from the moulds, cooled down in open air until reaching room temperature and finally cleaned. A sample was obtained from the bottom part of one wedge produced per batch to determine the chemical composition of each alloy. A combustion technique (LECO CS300) was used to determine the carbon and sulphur contents while an inductively coupled plasma mass spectrometer ICP-MS (Agilent 7500ce) was used for other elements after dissolving the metallic samples in a mixture of acids. Silicon contents were determined by gravimetric techniques. Chemical compositions for all significant elements are shown in Table 1.

Table 1. Chemical composition of the four alloys prepared in the present work (wt.%).

Alloy	C	Si	Mn	P	S	Cr	Ni
LGI	3.33	2.02	0.59	0.041	0.097	0.031	0.041
SGI-nd	3.21	3.93	0.16	<0.010	0.005	0.033	0.036
SGI-Dross	3.72	2.16	0.17	<0.010	0.007	0.035	0.039
SGI-CHG	3.20	3.96	0.15	<0.010	0.005	0.032	0.035
Alloy	Cu	Ti	Mg	Ce	La	Sn	Sb
LGI	0.46	0.017	---	---	---	0.056	---
SGI-nd	0.037	0.012	0.034	0.0042	0.0022	<0.005	0.0045
SGI-Dross	0.051	0.018	0.041	0.0038	0.0021	<0.005	0.0038
SGI-CHG	0.034	0.015	0.038	0.0035	0.0017	<0.005	<0.0005

The same wedges used to get the composition samples were then machined to produce tensile specimens with 10 mm in diameter (cylindrical section) and calibrated length of 50 mm, all of them obtained from the bottom areas of the wedges. On the SGI specimens, the ultimate tensile strength (UTS), the yield strength (YS) and the elongation at rupture (A) values were measured using a Zwick Z250 tensile testing equipment. In case of the LGI specimen, only the UTS parameter was determined as this alloy did not show detectable elastic zone and elongation at rupture. The SGI tensile specimens were produced with threaded ends and elongation values were determined by using a Zwick integrated transverse extensometer with 0.10 µm resolution. All tensile tests were made a constant strain rate of 2.5×10^{-4} s^{-1}.

The bottom parts of the second wedges were used to machine out two plate-like coupons with dimensions 35×15×3 mm. One side of each of those coupons was polished to obtain metallographic surfaces on which the microstructure of each alloy was inspected. Thus, graphite lamellas distribution and size for the LGI sample and nodularity (Nod) and nodule count (N) values for the SGI samples were determined. In a subsequent step, these polished surfaces were etched with Nital 5% reactant for 10-15 s and the contents of the matrix constituents were determined by visual inspection according to the corresponding standard [19]. The other coupons were used in the NDE studies.

The NDT test were performed with the help of dedicated magnetoacoustic emission (MAE) measurement system, designed and built at Gdańsk Tech. Measurement process and data storage were performed using embedded NI USB-6353 multifunction device responsible for voltage signal generation and data acquisition. The voltage signal, triangular in form, was fed to the current amplifier and then passed to the coils (4) of the electromagnet (see Fig. 1) with adaptable legs (3) and poles.
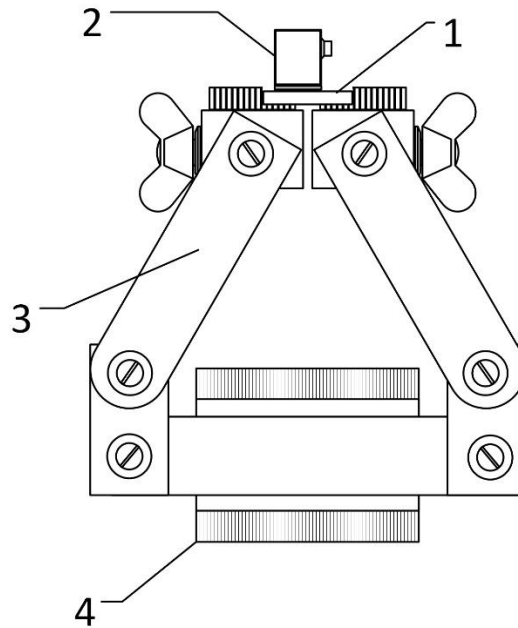
Fig.1 Measurement setup: 1 – sample; 2 – AE sensor (PZT); 3 – electromagnet; 4 - magnetising coil.

Such adaptability enables application of that electromagnet for a wide range of tested samples (in our case the samples (1) were at the lower dimension limit). The measurement set was controlled with the help of the software written in the LabVIEW environment. The software allowed for basic signal processing (calculation of rms-like envelopes and hence signal intensity), yet in order to perform more advanced signal analysis of the measured MAE noise signal it was necessary to store the whole signal, recorded with sufficiently high sampling frequency (in our case 2 MHz). The magnetoacoustic emission signal was measured with the help of five different piezoelectric transducers covering wide frequency range from about 20 kHz up to 500 kHz (as it was observed signal above 400 kHz was very weak). The main parameters of the transducers are given in Table 2. The maximum sensitivities for sensors VS30-V and R6a seem to be very similar yet the VS30 one is much more sensitive in 20-30 kHz range.

Table 2. The transducers used for the investigations.

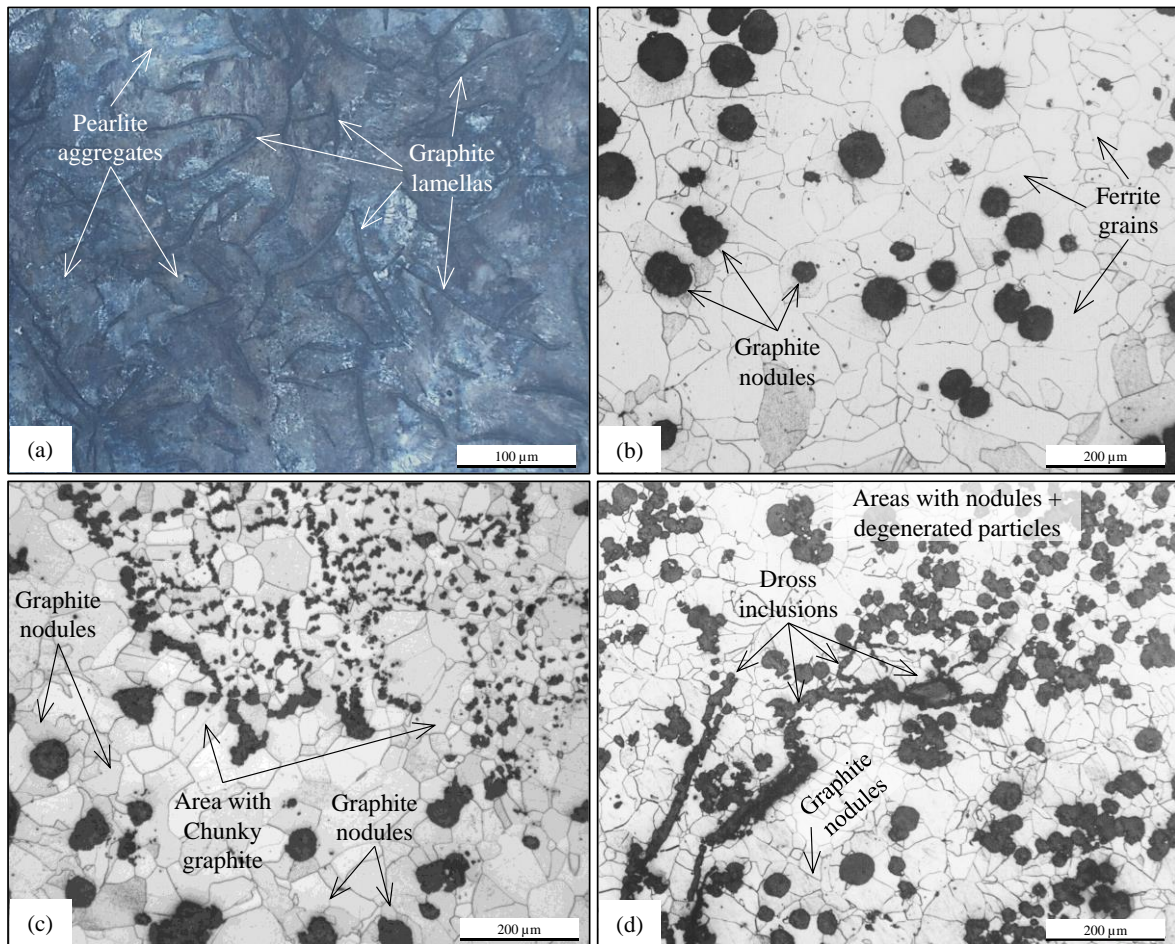| Manufacturer	Symbol	Freq. range [kHz]	Max. sensitivity - f_{max} [kHz]
Vallen	VS30-V	25-80	50
Vallen	VS45-H	20-450	100
Vallen	VS150 M	100-450	150
Physical Acoustic Co.	PAC R6α	35-100	55
Physical Acoustic Co.	PAC R30α	150-400	300

Fig. 2 Structural features found in: (a) the LGI sample, (b) the SGI-nd sample, (c) the SGI-Dross sample and (d) the SGI-CHG sample.

3. Results

3.1. Microstructure of the investigated alloys

The LGI sample contains the characteristic graphite lamellas (form I) randomly oriented, with sizes in the range 3-4 and c (Figure 2a). Pearlite aggregates showed the usual laminal structures composed by ferrite (Fe-α) and cementite (Fe$_3$C). For the three SGI samples, fully ferritic matrices are found with the grain boundaries revealed after etching the samples with the Nital 5 reactant. All these SGI show graphite nodules (rounded particles) with 20-100 μm in diameter. Notice that nodularity values are higher than 90% only for the sample SGI-nd without any graphite degeneration or inclusions (Figure 2b). As expected, relevant amounts of CHG and of Dross inclusions are present in the samples SGI-CHG (Figure 2c) and SGI-Dross (Figure 2d), respectively. For the first case, the areas occupied by the defect represented about 30% of the inspected areas while this percentage increased up to about 40% in case of the sample with Dross inclusions. In sample SGI-Dross, it is worthy to point that Dross inclusions appear like elongated inclusions present in the ferritic matrix (see Figure 2d). Moreover, important areas with degenerated graphite particles and small nodules are surrounding these Dross inclusions as it is commonly found in samples with this casting defect.

Table 3. Results from the metallographic inspections made on the three SGI alloys.

Alloy	Nod (%)	N (mm^{-2})	Ferrite (%)	Pearlite (%)
SGI-nd	>90	35-55	100	0
SGI-CHG	40-50	45-60	100	traces
SGI-Dross	50-60	80-110	100	0

3.2. Tensile properties

Table 4 shows the results obtained from all the tensile tests carried out on the specimen prepared from each alloy. It is clear that the LGI sample shows the lowest UTS value as graphite particles are lamellas or flakes with high stress concentration in their tips if compared to graphite nodules present in the SGI-nd sample.

Table 4. Tensile results from the tested specimens.

Alloy	UTS (MPa)	YS (MPa)	A (%)
LGI	248	---	---
SGI-nd	547	451	13.8
SGI-Dross	322	246	4.2
SGI-CHG	539	455	11.1

When comparing the three SGI samples, one must consider that SGI-nd and SGI-CHG are ductile irons with high silicon contents (close to 4 wt.%) while this element is present in SGI-Dross at a content of 2.16 wt.%. As silicon strongly increases ferrite hardness, the comparative low UTS and YS values obtained for the SGI-Dross specimen in Table 4 cannot be exclusively assigned to the presence of Dross inclusions in that sample as silicon content is close to the half of that present in the two other SGI samples. However, the negative effect of Dross inclusions is much more evident for the elongation at rupture which should increase in the low-silicon SGI-Dross alloy with respect to the samples with high silicon content. On the contrary, the elongation data shown in Table 4 do show an important reduction in this parameter for the SGI-Dross specimen likely due to this type of inclusions.

In case of CHG defect, a comparison of tensile properties of samples SGI-nd and SGI-CHG shows similar UTS and YS values and a slight decrease in the elongation at rupture value for the last alloy. These results were already observed by Sertucha et al. [6] and they concluded that the negative effect of CHG on tensile properties of high silicon ductile irons is not relevant though it is not the case for the A parameter, the decrease of which may be significant. For these reasons, it is considered that both CHG and Dross inclusions are not acceptable defects in commercial ductile iron castings according to the customers' requirements.
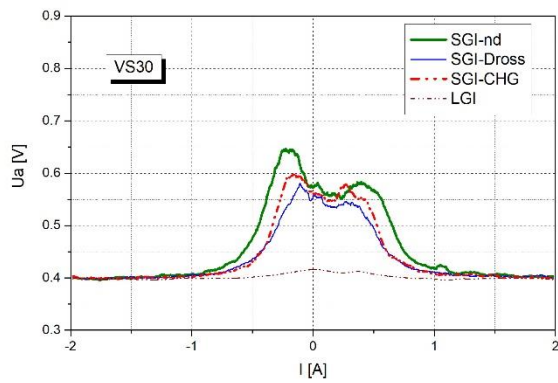
Fig. 3 MAE signal envelopes for the investigated samples – sensor VS30
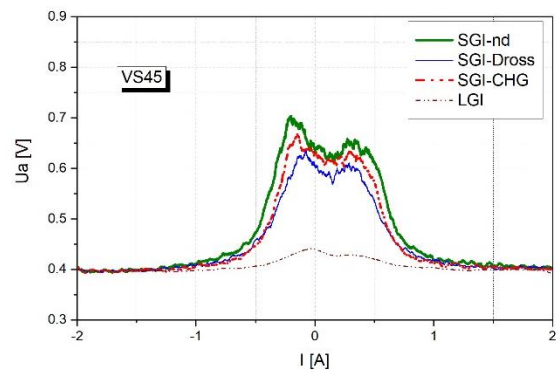

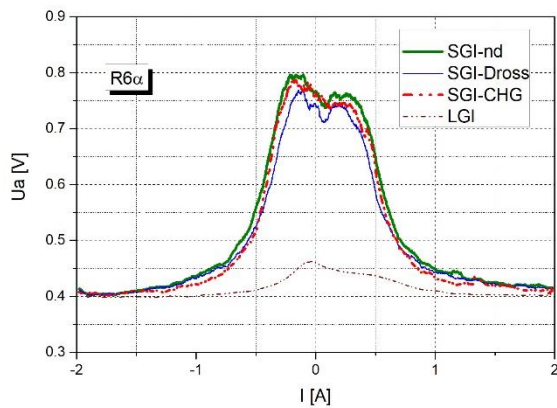Fig. 4 MAE signal envelopes for the investigated samples – sensor VS45

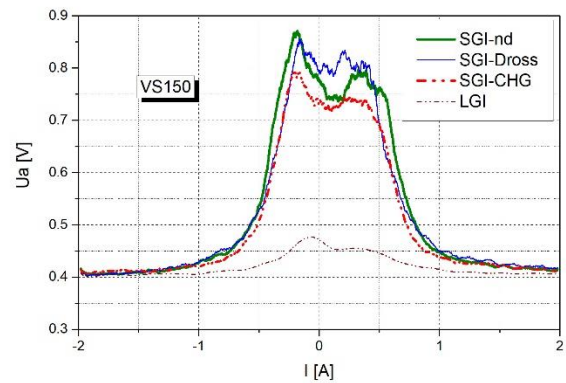Fig. 5 MAE signal envelopes for the investigated samples – sensor R6α

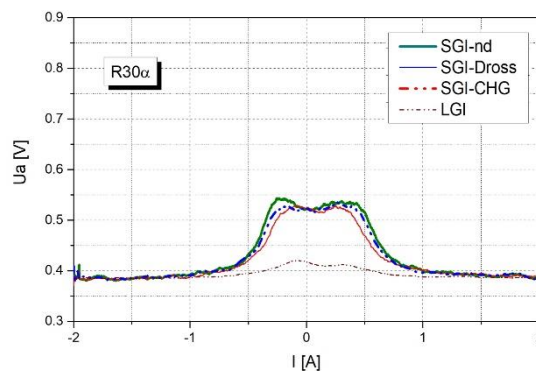Fig. 6 MAE signal envelopes for the investigated samples – sensor VS150

Fig. 7 MAE signal envelopes for the investigated samples – sensor R30α

3.3. NDT invesigations

The examples of the MAE signal envelopes obtained for the investigated samples, with the help of various transducers are shown in Fig. 3 to Fig. 7. As can be seen the LGI sample has the MAE signal

intensity by far the lowest from all the signals obtained for the investigated samples. It makes the LGI sample easily discernible from the other, spheroidal ones. The distinguishing of other samples is more problematic, the envelopes for SGI-nd sample are the highest for all the transducers yet the difference is significant only for the VS30 one. For the others (especially PAC ones) the results are almost identical. In order to compare the results quantitatively the intensity of the signal was characterised with the help of the integral of the envelope (after the background level subtraction):

$$\text{Int(Ua)} = \int_{\text{Imin}}^{\text{Imax}} \sqrt{\text{Ua}^2 - \text{U}_{\text{noise}}^2} \; dI.$$
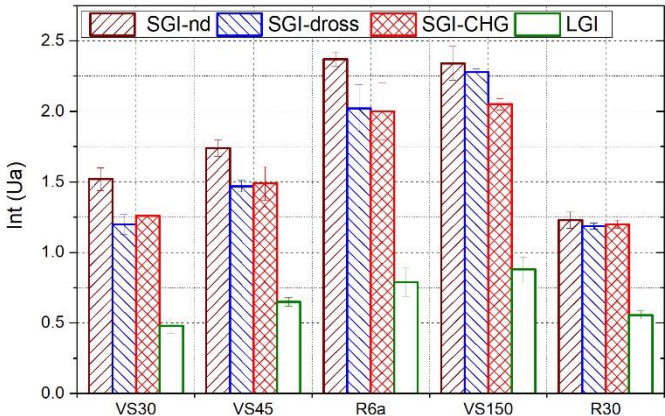

Fig. 8 MAE signal intensities obtained for the investigated samples and different AE sensors
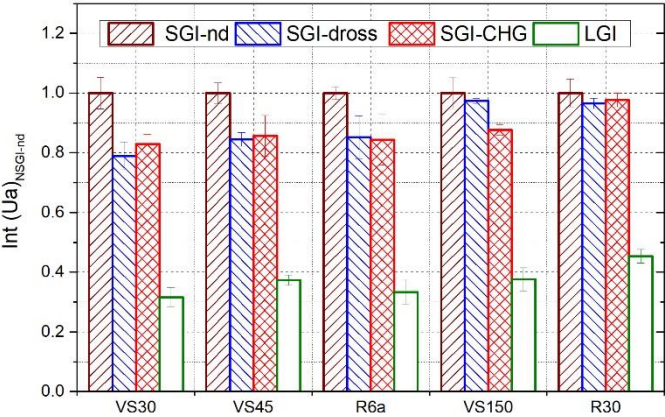

Fig. 9 Normalised MAE signal intensities obtained for the investigated samples. Horizontal line indicates the reference level

The results of such comparison are presented in Fig. 8. As can be seen they agree with the qualitative assessment on the basis of the envelopes. Definitely the biggest difference between SGI-nd/SGI-Dross and SGI-nd/SGI-CHG samples is observed for the VS-30 probe while the R30α sensor seems to be useless for telling apart of SGI samples. Yet even though the SGI-nd sample can be

10

correctly identified, with most of the sensors, in a set of samples like the investigated ones it does not seem to be possible do discern SGI-Dross and SGI-CHG samples analysing the intensity of the whole signal. In order to compare the relative difference between samples, the normalized MAE signal intensities are shown in Fig. 9. One can observe that the VS-150 seems to be the best option to distinguish samples SGI-Dross/SGI-CHG. It naturally confirms that, the LGI sample is easily discernible for every sensor.
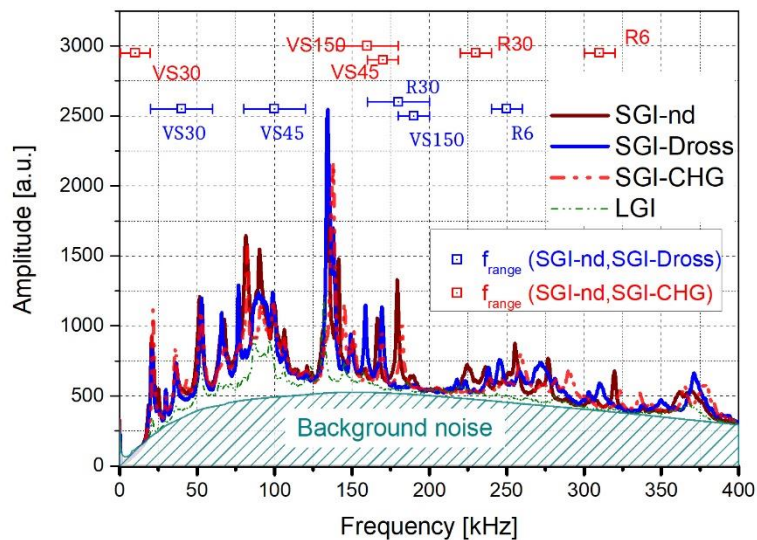

Fig. 10 Cumulative spectra (obtained for all the samples) of the investigated samples. Horizontal bars represent optimized (for either dross or chunky graphite detection) frequency ranges for the specified sensor.

The overall accumulated spectral intensities of the signals obtained with the help of five probes for all the investigated samples are shown in Fig. 10. As can be seen the signal has strong resonant components superimposed over a smooth background. The background noise to signal ratio is relatively high due to the small magnetising frequency (0.5 Hz) chosen. Such a choice of the frequency, even though not always possible (for high background noise level and weak emission), typically enables observation of more details of MAE signal envelopes. One can also observe that for, various frequencies, the spectral intensity of signals behaves in a different way hence the possibility of apparently contradictory results obtained with different transducers. The same effect can be also obtained for a single transducer with the help of digital filtering process (FFT - spectrum modification - FFT^{-1}). Being so, it is of the utmost importance to compare results obtained by various groups for similar transducers (and similar digital/analog filters). Since the FFT spectrum is very irregular it is not easy to obtain repeatable/reliable quantifiers. The most stable are integral parameters, being so we have investigated the behaviour of central frequency of the spectra – the results are shown in Table 5. As can be seen the frequency behaves in an opposite way to intensity – the highest one is obtained for

the LGI sample and the smallest for the SGI-nd one. Due to strongly resonant character of the sensors, it is impossible to determine the "natural" central frequency of the MAE signal yet the order of samples should be the same. It means that the LGI sample signal is composed of the shortest pulses, what suggests dominance of short jumps of domain walls during magnetisation.

Table 5. Central frequencies for all the samples.

Sample	SGI-ND	SGI-Dross	SGI-CHG	LGI
Central frequency [kHz]	187.0	195.5	194.5	206.2

Theoretically one could compare the spectral energy density of the signals on the basis of the plots like the ones in Fig. 10 simply by setting the integration boundaries and subtracting the background spectrum. This method is, however, not a good one for several reasons. Firstly, the FFT spectrum does not allow for assessment if the measured signal is truly the MAE one (we do not see signal envelopes) or is due to the background noise either of electrical nature or resulting from mechanically generated sounds (tapping, clicking, etc.). In all the cases the observed effect on the FFT envelope might be the same whereas observing signal envelopes we could easily tell if we observe the real increase of the MAE signal, abrupt change of background level or very sharp voltage peaks of high amplitude. The only plausible solution would be to use the FFT intensity plot for determination of promising frequency ranges f_{low} and f_{high}, (band pass filtering) remove unwanted components, perform the inverse transformation using the selected frequency range and then (if the reconstructed signal is all right) perform integration. Even though the difference in spectra of the signals are clearly visible, due to abovementioned issues, it is not so obvious how to find the optimal frequency range. To solve that problem we have created a dedicated post processing software using the LabVIEW environment. The program works in a loop scanning available frequency ranges, performing band pass filtering and calculating the Int(Ua) values. The scanning of frequency ranges proceeds in a stepwise manner i.e. the procedure starts with f_{low} =0 and f_{high}, equal to the value of the frequency step, defined by the user. In the second step f_{low} remains equal to 0 and f_{high} is increased by the frequency step value and then the scan proceeds with f_{low} frequency, being increased by frequency step value while it is less than f_{high}. In the next iterations procedure continues in a similar order i.e. set f_{low} =0, increase the f_{high}, increase f_{low} by the frequency step value while it is less than f_{high}. The procedure ends when the user defined maximum frequency is reached by f_{high} and the f_{low} frequency is maximized. The problem with calculations of the Int(Ua) values is due to the fact that the background noise level differs for every frequency range hence it must be determined automatically. In our case the background signal was determined on the basis of the signal intensity for magnetising current values close to extremum (for which the MAE signal is practically non-existent). It was however important to avoid start and end points as they are very often influenced by numerical artefacts introduced by FFT/FFT^{-1} procedures.

Instead the data from between the envelopes (two envelopes were always recorded) of the measured signal were used. The examples of calculated integral Int(Ua) as a function of filtering frequencies for investigated samples (scan up to 500kHz with the 20 kHz step) are shown in Fig. 11 (sample SGI-nd, sensor VS30) and Fig. 12 (sample SGI-Dross, sensor VS30).
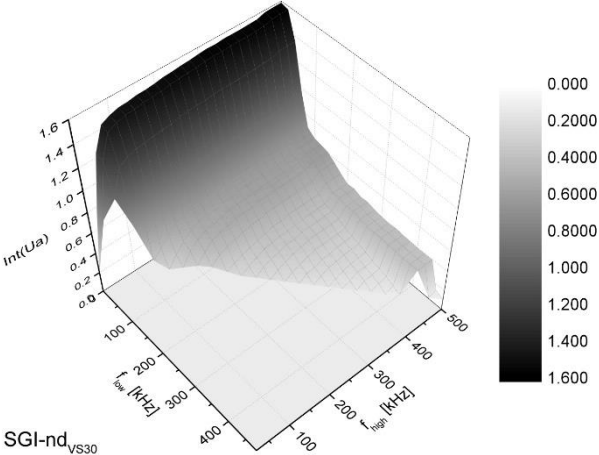

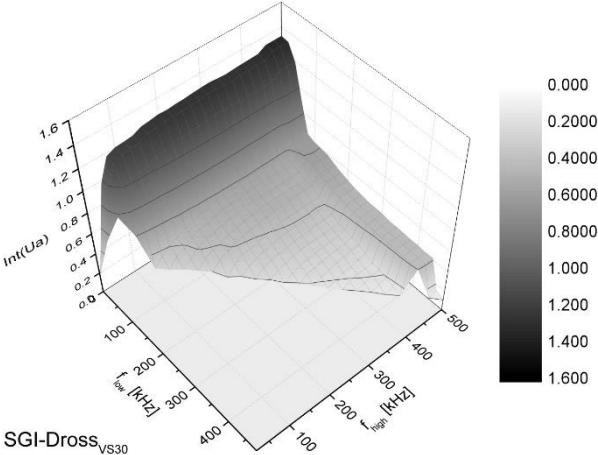Fig. 11 MAE signal intensity as function of low and high cut-off frequency – sample SGI-nd, sensor VS30

Fig. 12 MAE signal intensity as function of low and high cut-off frequency – sample SGI-Dross, sensor VS30

As the VS30 sensor is a relatively low frequency one for both samples we can observe maximum intensity for the lowest analysed f_{low} frequency range almost unaffected by the f_{high} value. As a result maximum change of the intensity on the first look seems to take place for this frequency range yet on the basis of direct comparison of two plots it may be not obvious what frequency range is the optimum one for discerning the samples. Assuming the similar level of relative data scatter we decided to look for the maximum relative intensity change taking the values for the reference sample (SGI-nd) as a normalising factor. For this purpose for every sensor a relative intensity change map, calculated for analysed pairs of samples (SGI-nd, SGI-Dross) and (SGI-nd, SGI-CHG) was created. The example of such map is presented in Fig. 13 in which the samples (SGI-nd, SGI-Dross) are compared. In this case the

13

results are in agreement with initial predictions i.e. the best frequency range for comparison of those samples is a low frequency narrow band. More interesting situation is observed for other sensors. The intensity map for sensor VS150 and SGI-nd sample is shown in Fig. 14 whereas the relative intensity difference for this sensor and (SGI-nd, SGI-Dross) samples is shown in Fig. 15.
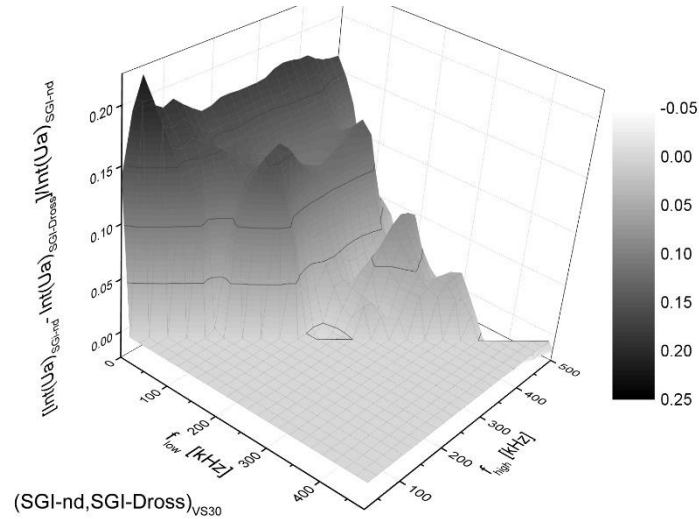

Fig. 13 Relative MAE signal intensity difference as a function of low and high cut-off frequency – samples (SGI-nd, SGI-Dross); sensor VS30
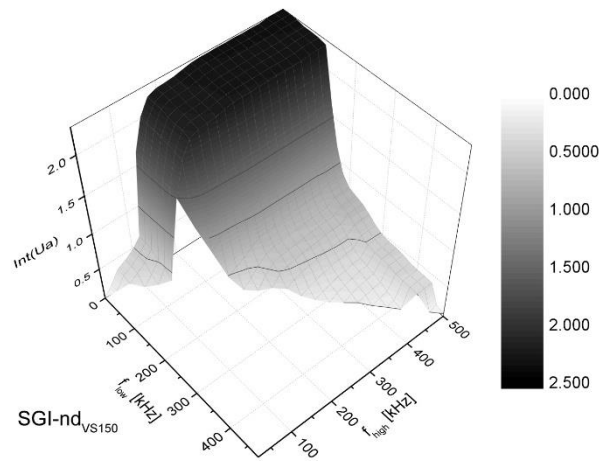

Fig. 14 MAE signal intensity as a function of low and high cut-off frequency – sample SGI-nd, sensor VS150

As can be seen there is possibility of obtaining both positive and negative change depending on the chosen frequency range – such behaviour leads to completely different results for various frequency ranges yet it suggest a possibility of differentiating various casting defects (dross inclusions and CHG) in investigated samples by adjusting the analysed frequency range. It is also worth noting that the obtained maximum relative change is even bigger than the one obtained for seemingly most sensitive sensor (without band pass filtering). For both pairs of samples (SGI-nd, SGI-Dross) and (SGI-nd, SGI-CHG) the obtained maps were analysed for each of the sensors and frequency ranges allowing for best discerning of the investigated samples were determined (leaving out the results for LGI sample as the

14

results for that sample are so different from the other ones that the optimisation procedure is unnecessary).
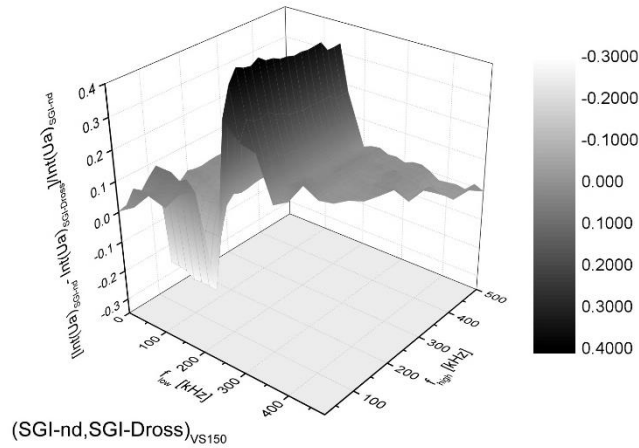

(SGI-nd,SGI-Dross)$_{VS150}$

Fig. 15 Relative MAE signal intensity difference as a function of low and high cut-off frequency – samples (SGI-nd, SGI-Dross); sensor VS150

The integrals of the signals for the investigated samples were calculated (for every frequency range the integrals for all the SGI samples were also determined in order to assess if the given range could be used for differentiating all three samples, not only the given pair). In addition to that the frequency ranges have been determined for which the highest difference between results between SGI-Dross and SGI-CHG samples is observed and for those frequencies the integrals were calculated too.
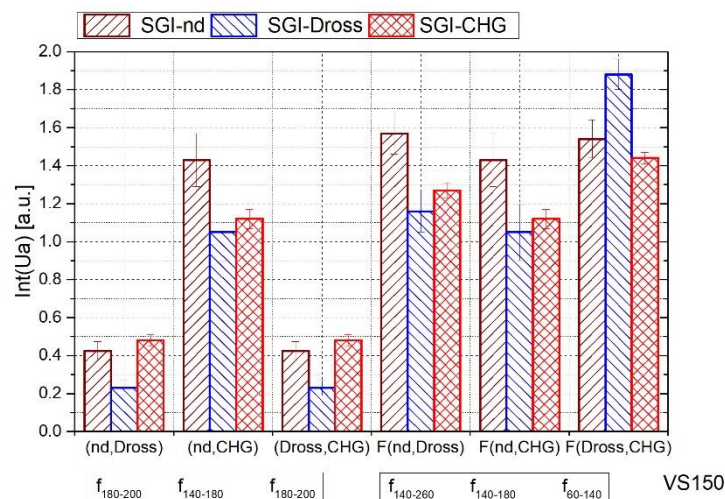

Fig. 16 MAE signal intensities for VS150 sensor. The sample pairs like (nd,Dross) identify the samples for which is obtained either maximum of relative difference or of figure of merit – in the latter case the letter F is added - F(nd,Dross) etc.. Below the plot filtering frequency ranges are indicated.

Examples of the obtained results (for VS150 sensor) are shown as three first sets of columns in the Fig. 16. The box below the plot indicates the frequency ranges used in calculations. As can be seen two of three sets are obtained for narrow frequency ranges giving small signal intensities. Such small signals may be difficult to detect in non-laboratory conditions so we have decided to look for the frequency

15

ranges for which the figure of merit was the product of relative change and signal intensity. The obtained results are shown as the right three sets of columns (sample pairs with letter F). As could be predicted the frequency ranges broadened in case of previously narrow ones and measured intensifies increased significantly. For the (SGI-nd, SGI-CHG) it turned out that the optimal frequency range is exactly the same in both cases. Unfortunately, as predicted, the relative difference of intensities for different samples decreased significantly. In order to compare the results for different frequency ranges (for which the differences in reference sample signal intensity make comparison difficult) all the signals were normalised by the reference sample signal intensity for a given sensor and frequency range. The examples of the result are shown in Fig. 17 (again for VS150 sensor). As can be seen the difference between the samples SGI-nd and SGI-Dross can be in optimal conditions as high as almost 50% (with the scatter in the result of the order of 10%. The highest difference between SGI-nd and SGI-CHG samples is significantly smaller (a bit higher than 20%) yet it is still possible to discern the samples. As for the difference between SGI-Dross and SGI-CHG samples (analysing the full spectrum of the signal practically non-existent) the difference (observed for exactly the same frequency range to the one optimal for (SGI-nd, SGI-Dross) pair becomes very high – not only the SGI-Dross sample signal intensity is about 50% lower than the SGI-nd but for SGI-CHG it becomes about 13% higher than the reference.
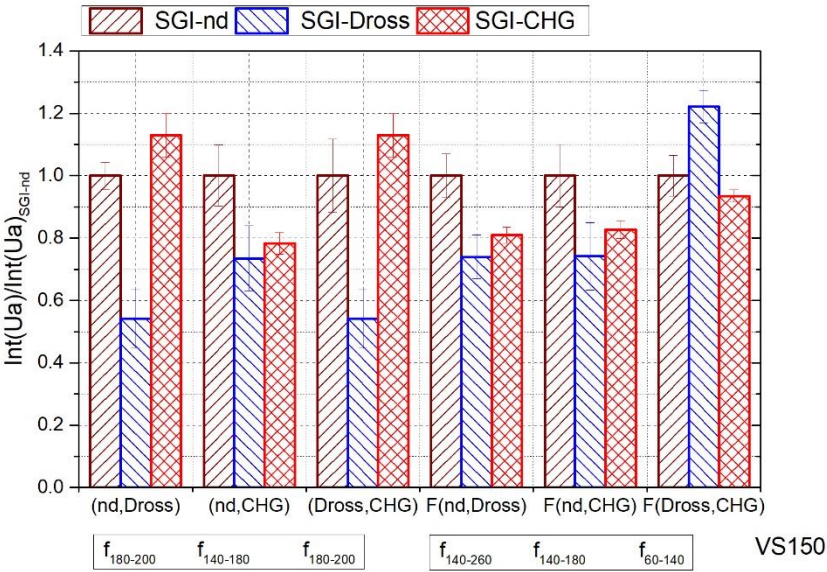

Fig. 17 Normalized MAE signal intensities for VS150 sensor

As for samples with the highest figure of merit the (SGI-nd, SGI-Dross) pair difference drops significantly yet is still higher (over 26%) than the highest difference observed for the nonfiltered signals (~21% for VS30 probe). As for the (SGI-nd, SGI-CHG) pair the selected frequency range is exactly the same as for the case of maximum intensity change. Finally for the pair (SGI-Dross, SGI-CHG) the optimum conditions are met in case when one of the sample signal intensities increases and the other

16

decreases relatively to the SGI-nd sample. In the best case the SGI-Dross sample signal intensity is about 22% higher than the SGI-nd one whereas for SGI-CHG it becomes about 8% lower than the reference.
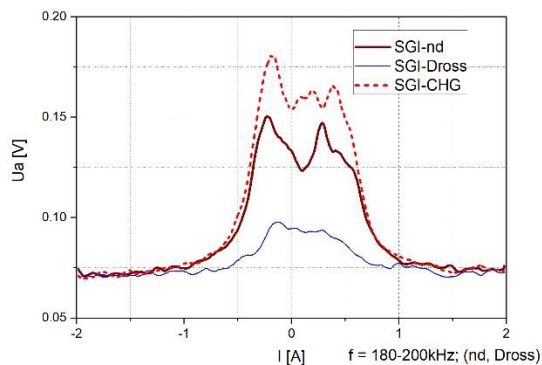

Fig.18 Reconstructed MAE signal envelopes after band pass numerical filtering (frequency range 180-200 kHz. The band optimized for discerning SGI-nd and SGI-Dross samples.
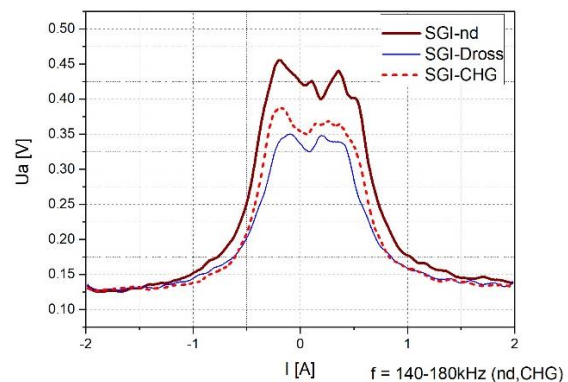
Fig.19 Reconstructed MAE signal envelopes after band pass numerical filtering (frequency range 140-180 kHz. The band optimized for discerning SGI-nd and SGI-CHG samples.

It should be noted that even though the intensities of the signals necessary for the best frequency ranges determination, were calculated automatically for all the investigated frequency ranges, yet after the completion of that process the MAE filtered signal envelopes were reconstructed with the help of inverse Fourier transformation (FFT^{-1}). The examples of such envelopes are shown in Fig. 18 and Fig. 19. As can be seen the envelopes have shapes typical for magnetoacoustic emission signals and the signals drop to the background noise level smoothly indicating that the calculated signal intensity encompasses the whole MAE generation process (the intensity of the MAE drops below detection level) and it is a reliable characteristic of the investigated samples. Comparing the obtained envelopes with the ones obtained for the whole spectrum one can observe a big difference – the samples become easily discernible, especially the SGI-Dross sample, the relative intensity of which is decreasing strongly for the selected frequency range. We would like to stress that only observation of the signal envelopes can guarantee that the measured signal is truly the MAE signal, not the background acoustic or electrical noise. In principle the background might be determined independently by measuring the signal for the sensor placed on the sample without the magnetising current, yet still there will be possibility that some noise source appears during the measurements. It was shown that if the background noise is determined correctly the true intensity can be calculated in a repeatable manner. As can be seen the changes of the signals are very significant. In general, taking into account central frequencies one would expect that the SGI-nd sample should have mostly low frequency component (big, regularly spaced carbides). However the data form Fig.18 show that signal for SGI-CHG is higher, as predicted, yet it is not true for SGI-Dross, What is more, in Fig. 19 the SGI-

17

Dross signal is by far the smallest. It may be due to the fact that this particular graphite distribution (see Fig. 2) is strongly bimodal and it is probable that we observe local minimum of the signal. It confirms the fact that the character of graphite morphology differences in combination with resonant sensors make *a-priori* prediction of optimum measurement parameters very difficult and the automatization and optimization of the data analysis process would be very useful.
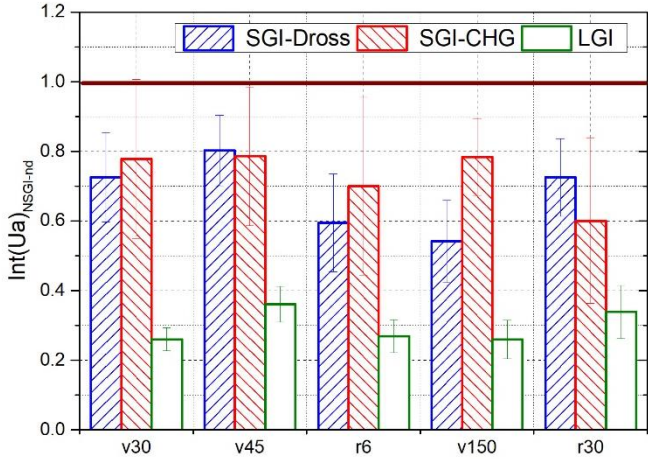

Fig. 20 Relative MAE signal intensities for frequency ranges resulting (for SGI-Dross & SGI-CHG samples) in the highest difference between specified sample and the reference one (SGI-nd). For the LGI sample the highest S/N ratio was searched for.
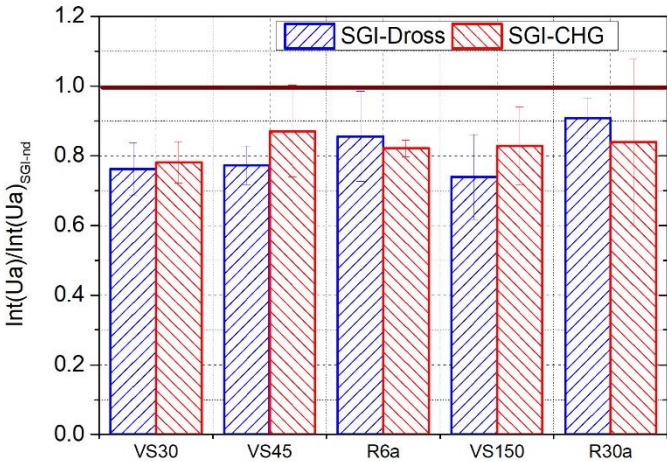

Fig. 21 Relative MAE signal intensities for frequency ranges resulting in the highest product of intensity and relative difference between specified sample and the reference one (SGI-nd).

The analysis of that kind (searching for both, maximum relative difference and highest figure of merit) was performed for every sensor and the frequency ranges obtained while looking for the highest relative difference are shown in upper part of Fig. 10 (scatter plots). All the results are summarised in Fig. 20 – Fig. 22.
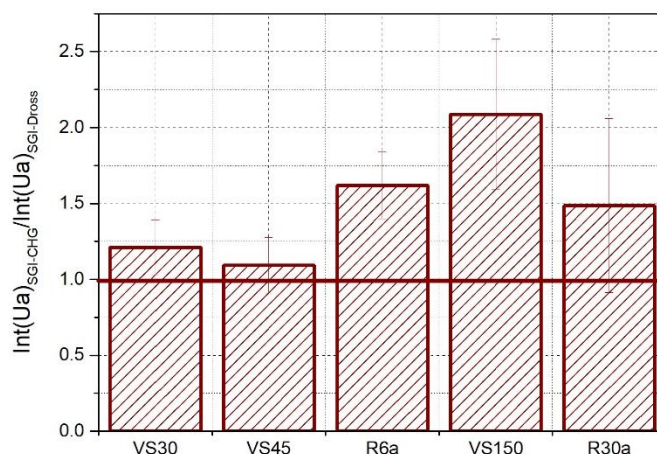
Fig. 22 Relative MAE signal intensities for frequency ranges resulting in the highest difference between samples SGI-Dross & SGI-CHG.
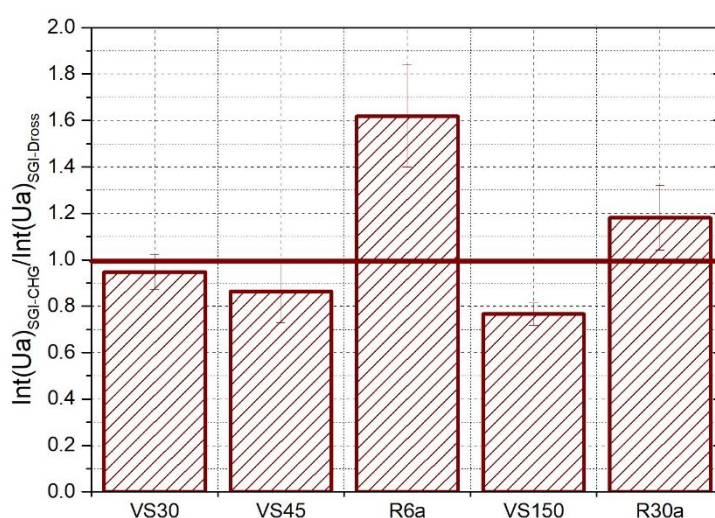

Fig. 23 Relative MAE signal intensities for frequency ranges resulting in the highest product of intensity and relative difference between samples SGI-Dross and SGI-CHG.

Fig. 20 compares the signals (normalised relative to the SGI-nd sample) obtained for various samples for the frequency ranges for which the highest relative changes were measured for every sensor used. It must be noted that for a given sensor, different frequency ranges were used for SGI-Dross and SGI-CHG (the signals had to be normalised by the adequately filtered SGI-nd sample signal intensity). The LGI sample did not undergo optimisation procedure on the basis of the search for the maximum relative signal difference (there was no use to do it as the sample is easily discernible) instead of that, because LGI signal is relatively weak, the frequency ranges for which the S/N ratio is highest were found. The thick horizontal line represents the reference (SGI-nd) sample signal intensity. The error bars are so extensive since in the picture they do not represent the uncertainties for measured signals but their ratio to the reference level. Being so as long as they do not exceed the ratio = 1 horizontal line we can assume that the samples are discernible.

19

One can see that the LGI sample has completely different MAE signal intensity and it is very easy to discern it from the other samples. The SGI-Dross sample can be discerned from the reference sample (SGI-nd) with the help of every sensor applying proper signal filtering, the highest difference being observed for VS150 sensor. As for the SGI-CHG sample the difference between that sample and the reference one can be most easily detected with the help of relatively high frequency probe R30α, since in that case the intensity drops by 40%, yet this is observed for a narrow frequency band suggesting the presence of some local minimum of SGI-CHG signal. This is also confirmed by relatively high scatter of data in this case. Since the optimum frequency ranges for some sensors were narrow (resulting in low signal intensity) the above mentioned maximum figure of merit was also sought after and the results (obtained in a way described in the case of Fig. 20) are shown in Fig. 21. The increased signal intensities resulted in decreasing scatter of results, hence even though the difference between signals measured for the reference and other samples decreased it still seems to be possible to discern the SGI-nd and SGI-Dross samples (~26% drop of relative intensity for VS150 sensor). Again for the (SGI-nd, SGI-CHG) pair the difference is smaller, yet three out of five sensors do enable to discern the SGI-nd and SGI-CHG samples (~18% drop of relative intensity for VS150 sensor). Finally the optimum parameters for the detection of the difference between SGI-Dross and SGI-CHG samples were determined for all the sensors and the ratio of SGI-CHG to SGI-Dross sample signal intensity was plotted in Fig. 22. As it can be seen the highest value of the ratio (higher than 2.0) is observed for VS150 sensor, but R6α probe also seems to appropriate for that task (ratio over 1.6). The figure of merit analysis have also been performed and the results are shown in Fig. 23. Surprisingly it turned out that for the R6α sensor the same frequency range was observed as in the case of maximum change determination so this sensor turned out to have the highest figure of merit. To conclude with, the results suggest possibility of using combination of three sensors R6a, R30a and VS150 for the comparison of the investigated samples, yet only the last one can be used as the only sensor for such tests, as it is suitable for discerning of all the samples.

3. Discussion

The case of SGI/LGI identification is not a problem using the MAE signal measurements. The difference is so significant that whatever the AE sensor we used and no matter if we filtered the signal or not the relative difference between lamellar and spheroidal graphite (reference sample) was of the order of 60%. It was also observed that the frequency range of the MAE signal generated in cast iron is very broad - from below 20 up to over 400 kHz. Being so one can use most of the commercially available AE sensors. However for some of them the samples with dross and CHG do not differ significantly. If the signals are too similar we are left with two options. Firstly we can change the sensor

(in our case a low frequency one turned out to be the most useful). Such result is in agreement with the fact that SGI-nd contains mainly big, widely separated graphite particles. The other option is to perform signal filtering, yet it is not so obvious what is the best frequency range. The problem arises from the fact that FFT spectrum is very sharp, probably due to mechanical resonances in the sensor/sample set. In addition the graphite size distribution may be very complicated, often bimodal (SGI-Dross). Being so we propose application of an automatic procedure capable of finding optimum frequency range. In our case the application of such procedure allowed for a very significant increase in the sensitivity since the observed relative difference between the reference and dross containing sample was over 50%. In addition to that it was shown that using filtering procedures one can discern the samples with the help of any tests sensor. And last but not least, it was possible to discern Dross and CHG containing samples – the goal that could be achieved using non filtered signals only for VS150 sample, yet in that case the reference and dross containing sample had almost the same signal intensity. It should be emphasized that band pass signal filtering in search for the frequency band resulting in the most dynamically changing signal may not give less dynamic change of analysed signal than analysis of full frequency range. In the worst case it may turn out that the optimum band is actually the whole band. The only drawback of the procedure is that the narrow filtering window may lead to low signal intensity and/or high level of uncertainty of the obtained results. Such problem can be avoided by using various figures of merit that can be easily calculated once the intensity vs (f_{low}, f_{high}) dependence is known. The program calculates automatically e.g. standard deviations for every (f_{low}, f_{high}) pair so one may look for frequency ranges with small stochastic scatter. The slowest procedure is the frequency scan which in our case (max. frequency 500 kHz, step 20 kHz) lasted about 10 minutes on a standard desktop PC.

The precision of the described frequency scan is limited by the frequency scan step – it cannot be decreased very much since a too small step would result in high scatter. The problem may be circumvented using the independent variables for frequency step (small value) and frequency range (higher value). The arising problem of calculation time could be dealt with the help of a two-step algorithm. In the first, rough scan the exact scanning area could be determined and then a high precision, slow scan could be done over selected frequency ranges.

4. Conclusions

First of all it is very easy to discern between the spheroidal and lamellar cast iron using MAE signal measurements, in this case no signal filtering is necessary. As for detection of flawed samples, i.e. discerning them from the flawless ones, it is a more challenging task. In this case frequency optimization (an appropriate choice of a sensor and filtering band) may greatly enhance the sensitivity

of the measurements. In our case it turned out that it is best to use a low frequency sensor. If one was to differentiate between dross/chunky graphite samples it is possible, but in this case it is best to use a middle range sensor. As a result of such investigations one can determine which sensor/frequency band is suitable for detecting any given microstructure changes. Two possible strategies are available. If the sensitivity was a most important factor one could use one sensor to detect flawed samples first and then, if necessary, use another one to determine the type of a flaw. However in industrial applications the most useful approach might be finding a sensor that using different frequency band filtering allows for both detection and qualification of the flaw.

References

[1] Tiedje N, Solidification, processing and properties of ductile cast iron, Mater. Sci. Technol., vol. 26, 2010, 505-514, https://doi.org/10.1179/026708310X12668415533649.

[2] ASM Handbook, Cast iron science and technology. Classification and basic types of cast iron, vol 1A in D. M. Stefanescu (Ed.) ASM International, Ohio, USA, 2017, 12–27,

https://doi.org/10.31399/asm.hb.v01a.9781627081795.

[3] Sertucha J, Lacaze J. Casting defects in sand-mold cast irons - An illustrated review with emphasis on spheroidal graphite cast irons, Metals, vol 12, 2022, 504, https://doi.org/10.3390/met12030504.

[4] Campbell J, Castings - second edition; Butterworth-Heinemann: Oxford, UK, 2003.

[5] Baer W, Chunky graphite in ferritic spheroidal graphite cast iron: formation, prevention, characterization, impact on properties: an overview, Int. J. Met., vol 14, 2020, 454-488, https://doi.org/10.1007/s40962-019-00363-8.

[6] Sertucha J, Artola G, de la Torre U, Lacaze J, Chunky graphite in low and high silicon spheroidal graphite cast irons - Occurrence, control and effect on mechanical properties, Materials, vol 13, 2020, 5402 https://doi.org/10.3390/ma13235402.

[7] Lacaze J, Magnusson-Åberg L, Sertucha J, Review of microstructural features of chunky graphite in ductile cast irons, Keith Millis Symposium on Ductile Cast Iron, 2013, 360-368, http://dx.doi.org/10.7494/jcme.2021.5.3.45.

[8] Cree J, Robles M, Hoover A, Thornberry N, Beckley S, Ductile Iron Front-End Ultrasonic Nodularity Determination Using Standard Coupons, Modern Casting, 2022, 29-33,

[9] G. Vertesy, T. Uchimoto, I. Tomas, T. Takagi, Nondestructive characterization of ductile cast iron by Magnetic Adaptive Testing, J. Magn. Magn. Mater. 322, 2010, 3117-3121, https://doi.org/10.1016/j.jmmm.2010.05.042.

[10] T. Matsumoto, T. Uchimoto, T. Takagi, G. Vertesy, Evaluation of Chill Structure in Ductile Cast Iron by Incremental Permeability Method, International Journal of Applied Electromagnetics and Mechanics, 52, 2016, 1599-1605, https://doi.org/10.3233/JAE-162106.

[11] Lord AE, Mason WP, Thurston RN (eds.): Physical Acoustics, p. 290. Academic Press, New York (1975).

[12] Shibata M, Ono K: Magnetomechanical acoustic emission—a new method for non-destructive stress measurement. NDT Int., 1981, vol 14(5), 227–234. https://doi.org/10.1016/0308-9126(81)90075-4

[13] Piotrowski L, Chmielewski M, Kowalewski Z, On the application of magnetoelastic properties measurements for plastic deformation level evaluation. J. Electr. Eng., vol 69(6), 2018, 502-506. https://doi. org/10.2478/jee-2018-0086.

[14] Buttle DJ, Scruby CB, Jakubovics JP & Briggs GAD Magneto-acoustic and Barkhausen emission: Their dependence on dislocations in iron, Philosophical Magazine A, 1987, 55(6), 717-734, 10.1080/01418618708214379.

[15] Sablik MJ, Augustyniak B, Piotrowski L, Modeling incipient creep damage effects on Barkhausen noise and magnetoacoustic emission, J. Magn. Magn. Mater., 272–276, 2004, E523-E525, https://doi.org/10.1016/j.jmmm.2003.11.297.

[16] Dhar A, Clapham L, Atherton DL, The influence of pearlite on magneto-acoustic emission in plain carbon steels, Acta Metall. Mater., 41(1) 1993, 199-204, https://doi.org/10.1016/0956-7151(93)90351-R.

[17] Piotrowski L, Chmielewski M, Augustyniak B, On the correlation between magnetoacoustic emission and magnetostriction dependence on the applied magnetic field, J. Magn. Magn. Mater., 410, 2016, 34-40, https://doi.org/10.1016/j.jmmm.2016.03.018.

[18] EN 1563, Founding, Spheroidal graphite cast irons (2011).

[19] ISO 945-1, Microstructure of cast irons - Part 1: Graphite classification by visual analysis (2017).